Research Article

Peipei Du, Yuzhu Zhang, Yue Long*, and Lei Xing

Preparation of $CaO–SiO_2–Al_2O_3$ inorganic fibers from melting-separated red mud

https://doi.org/10.1515/htmp-2022-0272
received July 30, 2022; accepted March 20, 2023

Abstract: To investigate the feasibility of preparing $CaO–SiO_2–Al_2O_3$ inorganic fibers with melting-separated red mud, the properties of the melting-separated red mud were analyzed by X-ray fluorescence, X-ray diffraction, and differential thermal-thermogravimetric analyses. The composition of the melting-separated red mud satisfied the requirements for the composition of inorganic fibers. During the melting of the melting-separated red mud, tetrahedral skeleton fracture reactions occurred at 1,234°C, anionic group reverse binding occurred at 1,250°C, and there was no other obvious reaction peak during the whole melting process, which lasted for 51 min. The minimum suitable fiber forming temperature of the melting-separated red mud melt was 1,433°C, which was 83°C greater than its crystallization temperature, 1,350°C. Within this temperature range, the activation energy of particle movement in the melt was 1008.65 $kJ·mol^{-1}$, and the melt exhibited good fluidity. Considering the temperature distribution corresponding to the melting properties of the melting-separated red mud, $CaO–SiO_2–Al_2O_3$ inorganic fibers could be prepared when the melting-separated red mud was subjected to component reconstruction by increasing the silicon content, reducing the aluminum content, and adding a moderate amount of calcium. Quartz sand and light burnt dolomite were used as modifying agents and inorganic fibers were prepared under laboratory conditions. The fibers prepared from the modified melting-separated red mud by adding different amounts of melting-separated red mud had smooth surfaces and were arranged in a crossed manner at the macroscopic level. Their color was grayish-white, and small quantities of slag balls were doped inside the fibers. With an increase in the amount of melting-separated red mud from 50 to 100%, the average fiber diameter increased from 5.5 to 8.0 μm, and their slag ball content increased from 2.9 to 6.0%. Overall, under laboratory conditions, when the amount of melting-separated red mud added was 50%, dolomite was 22.5% and quartz sand was 27.5%, the performance of the fiber was the best.

Keywords: melting-separated red mud, property, $CaO–SiO_2–Al_2O_3$ inorganic fiber, feasibility

1 Introduction

Red mud is the waste residue produced during alumina processing. Its name is based on the red color derived from its high iron oxide content [1–4]. The unit output of red mud is affected by the ore grade, production method, and technical level [5–7], with 1.0–1.8 t red mud being the byproduct of the production of 1 t of alumina [8,9]. Red mud contains many useful minerals and its main components are SiO_2, Al_2O_3, CaO, Fe_2O_3, MgO, and small amounts of potassium, sodium, titanium aluminum, rare earth elements, and other elements [10]. At present, the applications of red mud mainly include the extraction of valuable elements [11–13]. For example, red mud contains up to 50% iron oxides, which can be extracted using many methods, mainly pyrometallurgical methods [14–16]; a large amount of titanium, aluminum, and rare earth elements can also be extracted by hydrometallurgical methods [17]. Inorganic fibers are prepared from silicates by melting and fibrillation processes. They have a specific chemical composition range: 36–42 wt% SiO_2, 28–47 wt% CaO, 3–12 wt% MgO, and 9–17 wt% Al_2O_3. High-quality inorganic fiber products have excellent thermal and sound insulation characteristics and are widely used in aviation applications, automobiles, shipbuilding, electronic technology, the chemical industry, construction, agriculture, medicine, and other fields [18–20]. Melting-separated red mud is the residue when the iron is removed from Bayer red mud based on direct reduction and melting, and its main components are Al_2O_3, SiO_2, CaO, and MgO.

* **Corresponding author: Yue Long,** School of Metallurgy and Energy, North China University of Science and Technology, Tangshan 063009, China, e-mail: longyue@ncst.edu.cn
Peipei Du: School of Metallurgy, Northeastern University, Shenyang 110819, China
Yuzhu Zhang, Lei Xing: School of Metallurgy and Energy, North China University of Science and Technology, Tangshan 063009, China

Therefore, melting-separated red mud is a source of high-quality silicate materials that satisfy the conditions for preparing inorganic fibers. European scientists have prepared slag wool from slag that was directly obtained during the melting of red mud, and the process has passed a pilot plant [21]. However, the preparation of inorganic fibers with melting-separated red mud, as the main material has rarely been reported [22–27]. Preparation of high-quality $CaO–SiO_2–Al_2O_3$ inorganic fiber from melting-separation red mud is based on the extraction of the valuable element, iron, from red mud to realize the deep and high-value utilization of the tailings. It not only realizes the full-scale resource utilization of red mud but also increases the value of red mud products, and achieves good economic profits and social benefits. It is a new process that can realize high added value and the large-scale utilization of red mud, providing a practical and effective approach for the full-scale resource utilization of red mud. It is necessary to assess the feasibility of preparing $CaO–SiO_2–Al_2O_3$ inorganic fibers using melting-separated red mud. In this article, the composition, melting performance, viscosity, and crystallization performance of melting-separated red mud are deeply analyzed. Based on these properties of the melting-separated red mud, the differences between the preparation of raw materials of melting-separated red mud and $CaO–SiO_2–Al_2O_3$ inorganic fibers are analyzed. At the same time, the feasibility of preparing inorganic fibers from melting-separated red mud is confirmed by combining the experiment of preparing inorganic fibers from modified melting-separated red mud. The purpose of this study is to form the basic theory of directivity of preparing inorganic fibers from melting-separated red mud and provide theoretical guidance for the modification of melting-separated red mud and the preparation of high-quality inorganic fibers. It is of great environmental significance and scientific value to truly realize the full resource utilization of melting-separated red mud with high added value and further expand the field of comprehensive utilization of melting-separated red.

2 Materials and methods

2.1 Experimental raw material analysis

Melting-separated red mud, which is the residue that remains after red mud, is produced by the Bayer process and undergoes direct reduction and melting to remove iron, which was provided by the Aluminum Corporation of China. Its original particle size ranged from 3 to 5 mm, and it was crushed to less than 74 μm for use in this study.

The chemical composition of the melting-separation red mud was analyzed by using a RIGAKU ZSX Primus II X-ray fluorescence spectrometer. Samples were mixed evenly with boric acid and pressed into a solid sheet of 20 mm diameter and 4 mm thickness, and tablets were pressed. The mineral phase composition of the melting-separated red mud was analyzed by using a RIGAKU D/MAX X-ray diffraction spectrometer (XRD), in which the current was 40 mA, the voltage was 45 kV, the scanning speed was $5°·min^{-1}$, and the scanning angle was from 10 to 90°. The sample structure of the melting-separated red mud was analyzed by using a Bruker vertex 70 infrared spectrometer; 0.9 mg of the sample and 80.0 mg of KBr were fully crushed, mixed, and then pressed into tablets using the KBr tablet pressing method. The spectrum was measured at room temperature with 64 scans over a test range of 400–4,000 cm^{-1}. The physical and chemical changes in the melting-separated red mud during remelting were analyzed by using a NETZSCH STA449F3 high-temperature simultaneous thermal analyzer. The temperature was increased from 50 to 1,000°C at a heating rate of $30°C·min^{-1}$ and then to 1,500°C at a heating rate of $20°C·min^{-1}$ under an air atmosphere, and the reference material was α-$A1_2O_3$. The melting process of the melting-separated red mud was visually observed using an Rds-04 fully-automatic slag melting point-melting rate tester developed by the Institute of Ironmaking, Northeastern University. The melting-separated red mud (crushed to less than 74 μm) was evenly mixed with alcohol and then extruded into Φ3 mm × 3 mm cylindrical standard samples for analysis. The viscosity change of the melting-separated red mud during cooling was analyzed using an RTW-13 high-temperature melt physical property tester developed by Northeastern University. The melting-separated red mud (100 g) was put into a 50 mm × 240 mm corundum crucible, which was subsequently placed into the melt physical property tester for analysis. The temperature was increased to 1,500°C for 30 min and then slowly cooled at a $3°C·min^{-1}$ cooling rate. The crystallization behavior of the melting-separated red mud melt during cooling was simulated by the equilb module and phase diagram module of Factsage 7.1 thermodynamic software. The FToxid database and Scheil–Gulliver cooling mode are used in the simulation. The $SiO_2–Al_2O_3–CaO–Na_2O–TiO_2$ slag system, a five-component slag system, was analyzed in the simulation, and the simulation temperature range was 1,000–1,500°C. The crystallization behavior of the melting-separated red mud melt was investigated using a laboratory thermal

simulation test. A program-controlled energy-saving high-temperature resistance furnace was used to remelt the melting-separated red mud. The temperature was maintained for 30 min to ensure that the slag was fully melted after the temperature reached 1,500°C, cooled to a specific temperature near the theoretical crystallization temperature within the furnace, and finally, quenched. The melting-separated red mud melt was subjected to water quenching at different temperatures, and the morphology of the samples was analyzed using a Hitachi S4800 field emission scanning electron microscope and a scanning electron microscope (SEM). The surface of the sample was sprayed with gold before observation.

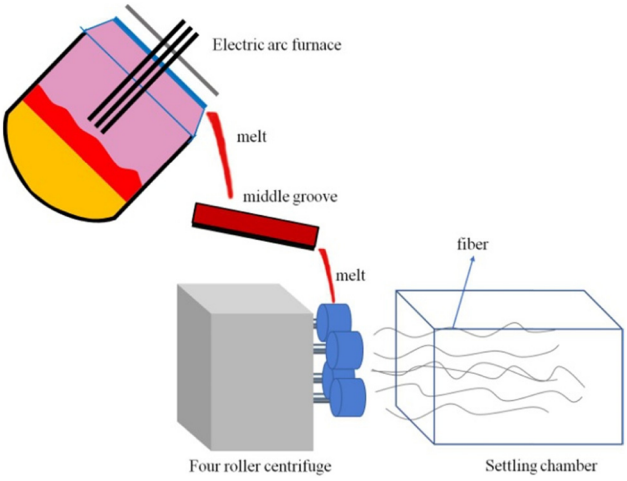

Figure 1: Schematic diagram of the experimental device and fiber-forming process.

2.2 Preparation of inorganic fibers

Inorganic fibers were prepared by the centrifugal method under laboratory conditions. The experimental device included a 100 kg DC electric arc furnace, a four-roll centrifuge, and fiber collection equipment. A diagram of the experimental equipment and fiber-forming process is shown in Figure 1. For fiber formation, 40 kg of the mixture was added to the electric arc furnace and heated to 1,500°C until it was completely homogenized. After the raw material was melted, sampling for water quenching treatment was done at an interval of 15 min, and the macro morphology of the water-quenched samples was analyzed to determine the holding time. If the surface of the sample was smooth and glassy, it indicates that the raw material is fully melted and homogeneous, and the holding time before fiber forming was appropriate. Then, the slag slowly flowed out of the electric arc furnace to the four-roll centrifuge to form fibers, which were collected. The rotating rated speeds of rollers #1, #2, #3, and #4 were 4,060, 4,640, 5,220, and 5,800 rpm, respectively. The speed of the centrifuge for fiber forming and the fan of the fiber collecting room were 2,800 and 1,800 rpm, respectively.

2.3 Properties of inorganic fibers

The macromorphology and micromorphology of the fibers were observed by stereomicroscope and SEM, respectively. The method to measure the diameter of a fiber was as follows: first, an appropriate amount of the fibers was weighed and sorted. Next, 1 cm bundles of fibers of equal length were cut and placed flat on a glass slide. Then, an appropriate amount of immersion solution was added to the fibers, and a needle was used to evenly sort the fibers, and ensure that they were close to one another and arranged in a single layer. The width of 100 fibers was measured by an optical microscope, and the average fiber diameter was obtained by a simple calculation. The slag ball content was measured with a slag ball content measuring instrument: the fiber and slag ball were separated by their buoyancy in water, and the slag ball content of the fiber was obtained using the following equation:

$$w = \frac{m}{m_0}, \tag{1}$$

where w is the slag ball content (%), m is the mass of the slag ball with a particle diameter greater than 0.25 mm as fiber (g), and m_0 is the mass of the fiber (g).

3 Results and discussion

3.1 Physicochemical property analysis of the melting-separated red mud

The chemical composition of the melting-separated red mud is affected by the raw materials, aluminum preparation process, and melting-separation process of red mud. The chemical composition of the melting-separated red mud in this experiment is shown in Table 1, and the apparent photos are shown in Figure 2 (grain sizes were less than 74 μm).

Considering the potential harmfulness of K, Cr, and other trace elements, the forms of the elements should be

Table 1: Main chemical components of the melting-separated red mud

Composition	Al_2O_3	SiO_2	CaO	Fe_2O_3	Na_2O	TiO_2	MgO	ZrO_2	SO_3	K_2O	Cr_2O_3	MnO	P_2O_5	Cl
Content (wt%)	32.311	27.261	10.616	7.558	11.159	7.234	2.140	0.295	0.709	0.297	0.193	0.131	0.084	0.013

strictly controlled in the process to treat melting-separated red mud and in the target products. Table 1 shows that the main elements in the melting-separation red mud were Al, Si, and Ca, followed by Fe, Na, Ti, Mg, and small amounts of Zr, S, K, Cr, and Mn. In addition, it contained trace amounts of P and Cl. Since the Cl content in the melting-separated red mud was extremely low (only 0.024%), this harmful element was ignored. Considering the safety of the chemical composition, it was feasible to prepare inorganic fibers from the melting-separated red mud.

Table 1 shows that the main components of the melting-separated red mud were Al_2O_3, SiO_2, Fe_2O_3, CaO, Na_2O, TiO_2, and MgO, which collectively account for more than 98% of the total components, and the chemical composition was similar to that of inorganic fibers. This result is consistent with the requirements of inorganic fibers in terms of raw material composition studied by Zhao and Li [25,28]. In addition, the red mud fiber is the product of the melt quenching treatment and it has an amorphous glass structure. According to irregular network theory, the main components of the melting-separated red mud are a primary network of SiO_2, an exterior network of CaO and Na_2O, and network intermediates of Al_2O_3, TiO_2, and MgO. Therefore, this melting-separated red mud satisfies the conditions for preparing inorganic fibers in terms of their chemical composition.

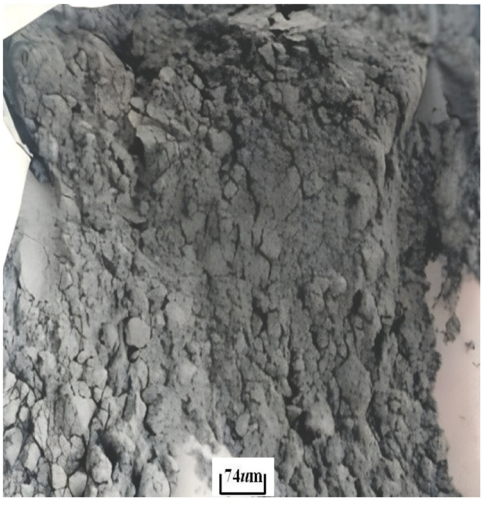

Figure 2: Melting-separated red mud.

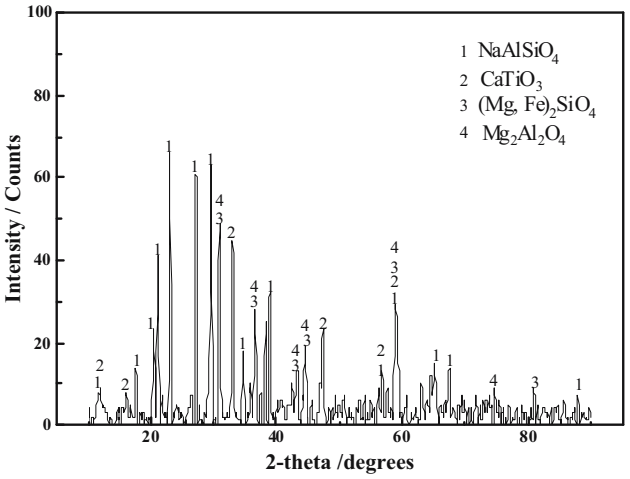

Figure 3: XRD pattern of the melting-separated red mud.

The XRD spectrum of the melting-separated red mud in Figure 3 shows that the phase composition of the melting-separated red mud mainly contained $NaAlSiO_4$, $CaTiO_3$, $Mg_2Al_2O_4$, and $(Mg, Fe)_2SiO_4$. The results are consistent with the XRD results for molten slag reported by Wang et al. [29]. $NaAlSiO_4$, the main crystalline phase, was a hexagonal framework of silicate, with short hexagonal columns and thick plate-like crystals, and the aggregates were granular or dense blocks [30].

The Fourier transform infrared spectroscopy (FTIR) spectrum of the melting-separated red mud is shown in

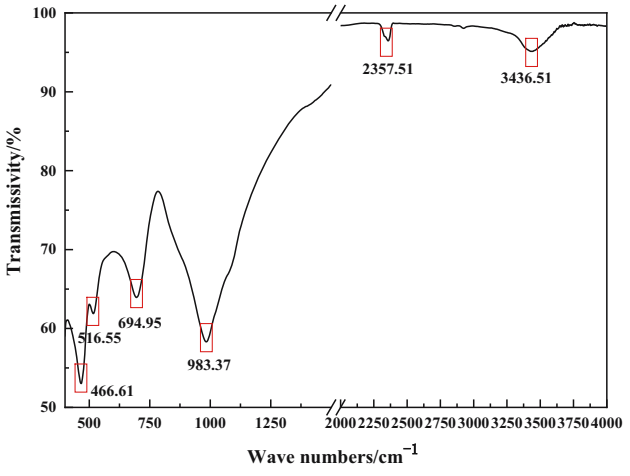

Figure 4: FTIR spectrum of the melting-separated red mud.

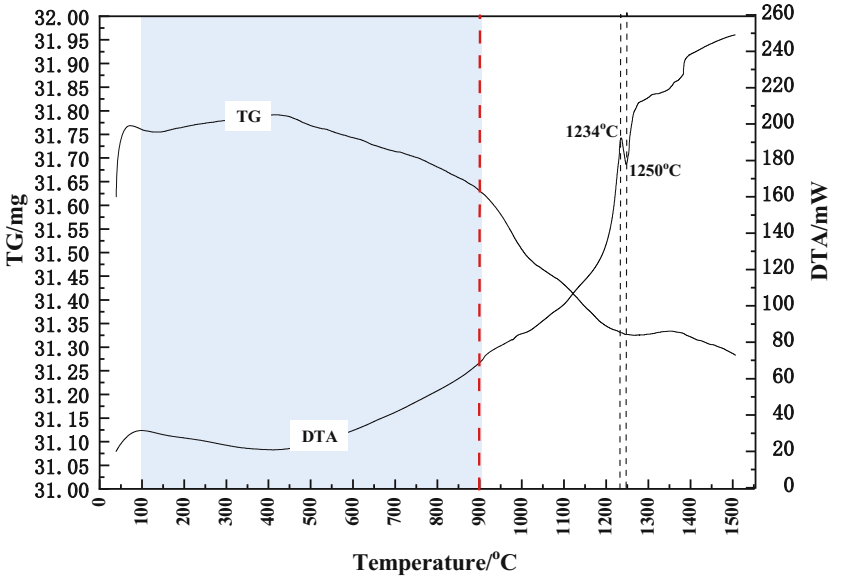

Figure 5: DT-TGA curves of the melting-separated red mud (in air).

Figure 4. The absorption band at 983.37 cm^{-1} in the low-frequency region was attributed to the stretching vibration of Si–O bonds in silica tetrahedra (SiO_4). This absorption band was generally asymmetric, which was attributed to the replacement of some of the Si by Al in the silica tetrahedron. The absorption band at 694.95 cm^{-1} was attributed to the vibrations of Si–O bonds and Al–O bonds, which were coupled with the vibrations of the tetrahedra (AlO_4, SiO_4) around the aluminum oxygen tetrahedron [31,32]. The absorption bands at 466.61 and 516.55 cm^{-1} were attributed to the bending vibration of the Si–O bond and the stretching vibration of the Si–O–Mg bond, respectively, and these vibrations were coupled with the translations of the Mg–O bond and the O–H bond [33]. The absorption bands at 3436.51 and 2357.51 cm^{-1} were attributed to the stretching vibration and bending vibration of water molecules, respectively [34]. Different vibrational frequencies of 466.61/516.55, 694.95, and 983.37 cm^{-1} roughly correspond to the absorption peaks of the structural units Q^0, Q^1, and Q^2, respectively. Q^n denotes the tetrahedral structure, and n, with possible values 0, 1, 2, 3, and 4, represents the number of bridges in each tetrahedral structural unit; a larger n value represents a lower nonbridging oxygen concentration in the structure and a higher degree of network polymerization [35–37]. Therefore, although the melting-separated red mud has a tetrahedral skeleton structure suitable for inorganic fibers, its overall structure is not stable, and the network polymerization degree is not high. Comparison with the results of Chang [23] shows that it is necessary to perform composition reconstruction when preparing inorganic fibers.

3.2 Melting property analysis of the melting-separated red mud

To better understand the physical and chemical changes in the melting-separated red mud during remelting, this process was analyzed using differential thermal-thermogravimetric analysis (DT-TGA). The results are shown in Figure 5.

The thermogravimetric (TG) curve in Figure 5 shows inconspicuous continuous mass loss in the temperature range of 100–900°C because the binding state and firmness of the bound water in the sample are different, and the bound water gradually evaporates with increasing temperature. There is an obvious mass loss of approximately 0.3%, in the TG curve in the temperature range of 900–1,250°C, and there is an obvious exothermic peak in the differential thermal analysis (DTA) curve at 1,234°C and an endothermic peak at 1,250°C. When the temperature exceeded 1,250°C, the TG curve did not significantly change, and the DTA curve had no obvious thermal effect.

The melting performance analysis results of the melting-separated red mud are shown in Figure 6. The temperature was 589°C, which is the initial state of the melting-separated red mud sample after it entered the furnace, and the sample height, h, was approximately 265 mm. When the solid-phase reaction occurred (equation (2)), the gas was released, the adsorbed water was removed, and the sample expanded. When the furnace temperature increased to 1,095°C, the expansion degree of the sample was maximal, and the height increased by $h/10$. The bound water and compounds

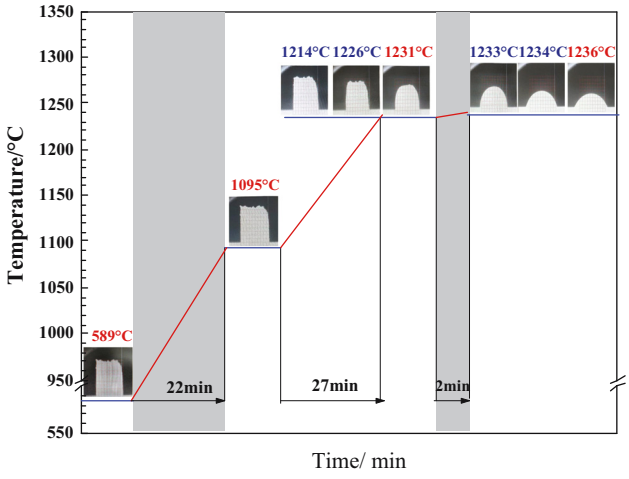

Figure 6: Melting process of the melting-separated red mud.

in the system are basically completely separated and decomposed (equations (3) and (4)), and the system generated gas, as determined by area *A* in Figure 6. With the interaction between SiO_2 and the other components, the Si–O sinter and low-temperature eutectic liquid phase formed, and the sample height gradually decreased. When the furnace temperature increased to 1,231°C, which is the denaturation temperature of the melting-separated red mud, the sample height was approximately 5/6*h*, and the formation of silicate in this system ended. With a further increase in temperature, the sample height more rapidly decreased, the reaction phase of the system changed to the solid phase and liquid phase, and the solid phase continuously melted to become the liquid phase, which indicates that the system entered the melt formation stage. This process ended when the system was completely converted into the liquid phase and reached equilibrium. The sample height was *h*/2, and the system temperature was 1,236°C, which indicates that this was the melting temperature of the melting-separated red mud. However, chain scission and decomposition of the tetrahedral skeleton in this system occurred when the temperature was approximately 1,234°C during this process. The entire melting process of the melting-separated red mud lasted 51 min, while the stage from raw material melting to silicate formation was 49 min, and the stage from the deformation temperature to a freely flowing melt was only 2 min. Therefore, the duration of the formation stage of silicate during the melting process of the melting-separated red mud should be decreased to reduce energy consumption. In Figure 6, the endothermic peak at 1,250°C indicates that the reverse combination of anionic groups occurred due to the increase in the number of degrees of freedom of the slag system caused by the increase in temperature. Overall, considering the thermal analysis and melting process of the melting-separated red mud, an insulation treatment should be carried out at approximately 1,234°C during the remelting process to ensure that the system fully melts:

$$Na_2CO_3 + CaCO_3 \rightarrow CaNa_2(CO_3)_2, \quad (2)$$

$$CaCO_3 \rightarrow CaO + CO_2, \quad (3)$$

$$CaNa_2(CO_3)_2 + 2SiO_2 \rightarrow Na_2SiO_3 + CaSiO_3 + 2CO_2. \quad (4)$$

3.3 Viscosity and fluidity analysis of the melting-separated red mud melt

Viscosity reflects the resistance to fluid convection. Convective movement occurred in the melt during fiber formation, so the melt viscosity influenced the fiber formation.

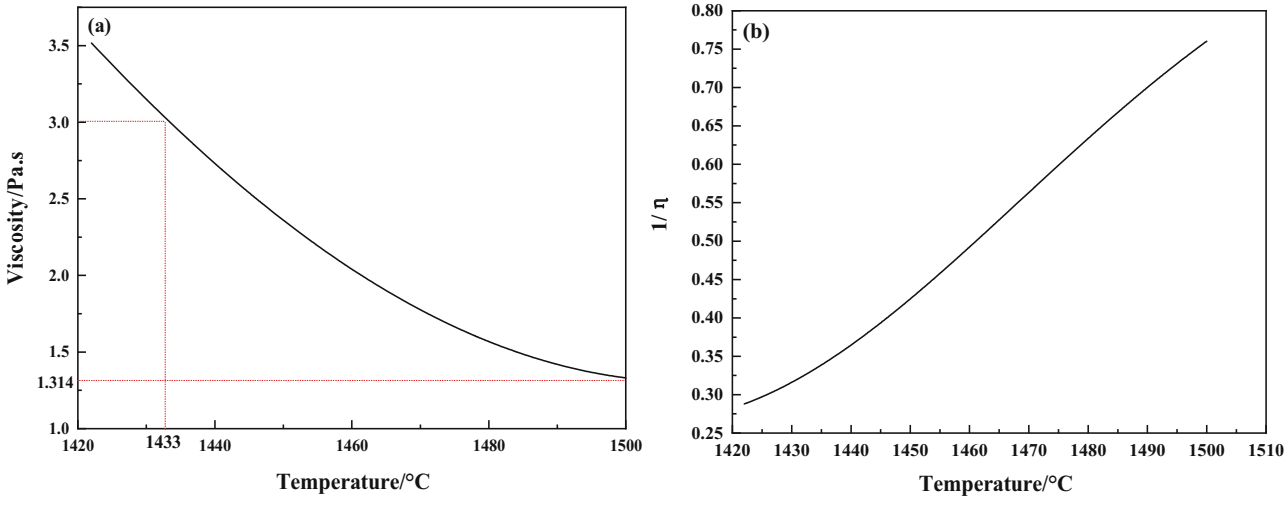

Figure 7: Flow property analysis of the melting-separated red mud melt: (a) viscosity–temperature curve and (b) fluidity–temperature curve.

The viscosity–temperature curve of the melting-separated red mud melt in Figure 7(a) shows that the viscosity of the melt gradually increased with decreasing temperature, and there was no obvious turning point, which is characteristic of a long slag. The suitable viscosity range of the melt during the formation of an inorganic fiber is 1–3 Pa·s [38]. Therefore, the temperature of the melting-separated red mud melt during the preparation of the inorganic fiber should not be less than 1,433°C.

The reciprocal of viscosity, $\varphi = 1/\eta$ (η is the viscosity), is used to characterize the mobility of the slag and is called the fluidity of slag. Greater fluidity corresponds to better slag mobility. The fluidity–temperature curve of the melting-separated red mud melt in Figure 7(b) indicates that in the high-temperature zone with a viscosity range of 1–3 Pa·s, the melt fluidity increased with increasing temperature, which is consistent with the slag viscosity analysis results.

In the appropriate fiber-forming temperature range, the particles in the melting-separated red mud melt are bonded to adjacent particles. Only when the particles have sufficient energy to overcome this barrier can they effectively move, which shows macro fluidity. With increasing system temperature, the particle ($[SiO_3]_n$, $[SiO_4]$, $[AlO_4]$) energy increased, and the number of particles that could overcome the force of adjacent particles increased. The thermal vibration of the particles increased, and the complex ions (low-molecular-weight polymers formed by short chains of silicon tetrahedra) underwent bond breaking and disintegration. The relationship between melt viscosity and temperature is characterized by the following equation [39]:

$$\eta = \eta_0 \exp(\Delta E/RT), \tag{5}$$

where ΔE is the activation energy of the particle movement in the melt, $J\cdot mol^{-1}$; η_0 is a constant related to the melt composition; R is the gas constant, $J\cdot mol^{-1}\cdot K^{-1}$; and T is the absolute temperature, K. After taking the logarithm of both sides of equations (5), Eq. (6) was obtained:

$$\log\eta = \log\eta_0 + \frac{\Delta E}{R}\frac{1}{T}. \tag{6}$$

According to equation (6), there is a linear relationship between $\log\eta$ and $\frac{1}{T}$, and the slope of the straight line (k) is $\frac{\Delta E}{R}$. In the high-temperature zone with a viscosity of less than 3 Pa·s, the fitting relationship between $\log\eta$ and $\frac{1}{T}$ of the melting-separated red mud melt is as shown in Figure 8, where R^2 is the coefficient of determination.

In the high-temperature zone with a viscosity of less than 3 Pa·s, there is an obvious linear relationship between $\log\eta$ and $\frac{1}{T}$ for the melting-separated red mud melt. Therefore, the anionic groups $Si_xO_y^{2-}$, which play a major role in the viscosity of the system, are not associated but are instead in a freely flowing state with irregular arrangements of small groups. The melt fluidity is good; in this temperature range, according to equation (6), with a slope of $k = 0.12132$ (as obtained from Figure 8) and the constant $R = 8.314\ J\cdot mol^{-1}\cdot K^{-1}$, the particle movement activation energy of the melting-separated red mud melt was calculated to be $1008.65\ kJ\cdot mol^{-1}$.

3.4 Crystallization property analysis of the melting-separated red mud melt

The main components of the melting-separated red mud are SiO_2, CaO, Al_2O_3, Na_2O, and TiO_2 as shown in Table 1; the influence of the above five main oxides on the melting-separated red mud phase was considered in the simulation calculations. The $SiO_2–Al_2O_3–CaO–Na_2O–TiO_2$ phase diagram is drawn with the phase diagram module of the thermodynamic software FactSage 7.1, as shown in Figure 9.

As shown in Figure 9, the area of the melting-separated red mud in the phase diagram was determined according to the melting-separated red mud composition. The carnegieite, nepheline, $CaTiO_3$, and melilite were generated during the crystallization process.

The simulation results of the Factsage thermodynamic software are shown in Figure 10. When the melt temperature decreased to 1,350°C, the carnegieite phase first precipitated in the melt, so this was the crystallization

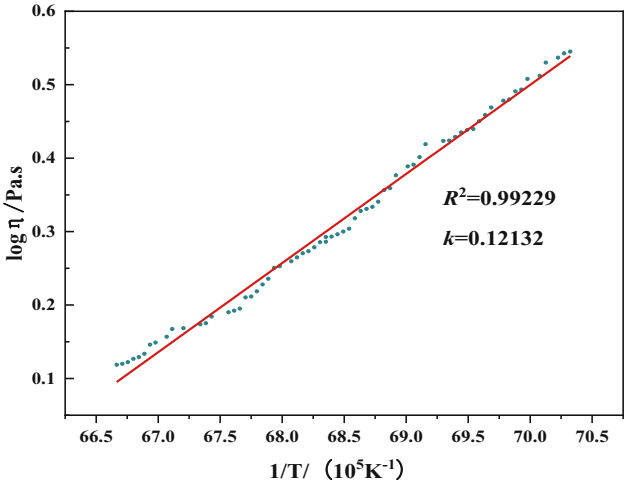

Figure 8: The fitting curve of $\log\eta$ vs $1/T$ of the melting-separated red mud melt.

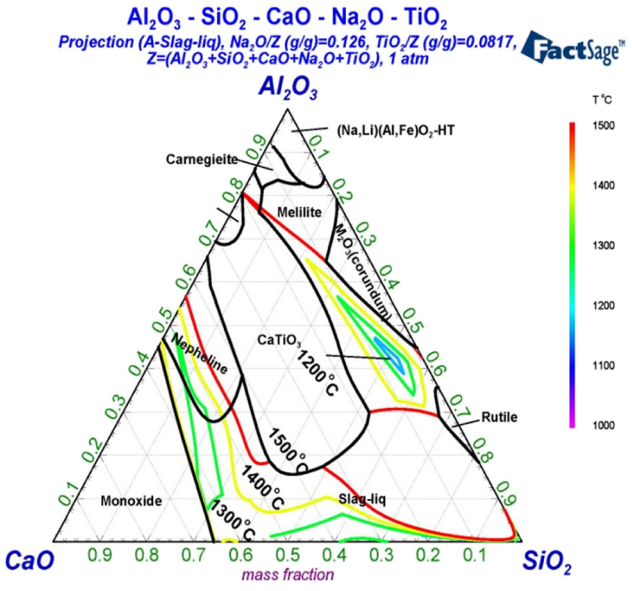

Figure 9: Phase diagram of SiO_2–Al_2O_3–CaO–Na_2O–TiO_2 (ωNa_2O = 11.159 mass%, ωTiO_2 = 7.234 mass%) obtained using FactSage 7.1.

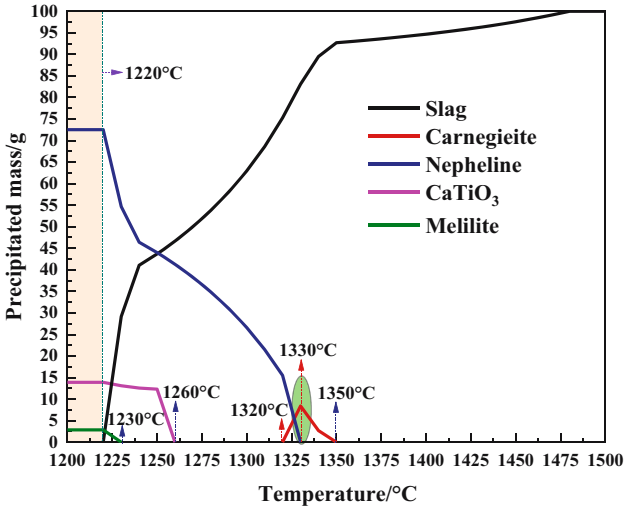

Figure 10: Simulation results for the crystallization behavior of the melting-separated red mud melt during cooling.

temperature of the melting-separated red mud melt. When the temperature decreased to 1,220°C, the phase precipitation reached thermodynamic equilibrium, and the amount of crystal precipitation did not change with decreasing temperature. Based on phase equilibrium theory, in the low-temperature zone below 1,220°C, the thermal energy of the melt molecular groups was not sufficient to overcome the required potential barrier for crystallization. Therefore, no crystal phase precipitated in the low-temperature zone after the melting-separated red mud melt was molded. In the temperature range of 1,220–1,350°C, when the temperature decreased to 1,330°C, the carnegieite phase began to transform to the carnegieite phase, and the carnegieite phase precipitated. When the temperature decreased to 1,320°C, all the carnegieite phases transformed into the carnegieite phase. The $CaTiO_3$ phase and melilite phase precipitated from the melt at 1,260 and 1,230°C, respectively. The nepheline phase had the highest precipitation content (72.528 g/100 g), followed by the $CaTiO_3$ phase (13.907 g/100 g).

To verify the correctness of the Factsage simulation results, the micromorphology of the water-quenched samples was analyzed by SEM. Figure 11 shows the SEM results where only a few crystals were present in the sample when the melt was subjected to water quenching at 1,350°C. At 1,220°C, there were many orderly arranged crystals in the sample, and the crystallization of the melt was complete.

In conclusion, the melting temperature of the melting-separated red mud was 1,236°C, and the minimum suitable fiber-forming temperature and crystallization temperature of the melting-separated red mud melt were 1,433 and 1,350°C, respectively. The minimum suitable fiber-forming temperature of the melting-separated red mud melt was 83°C higher than its crystallization temperature, which was much

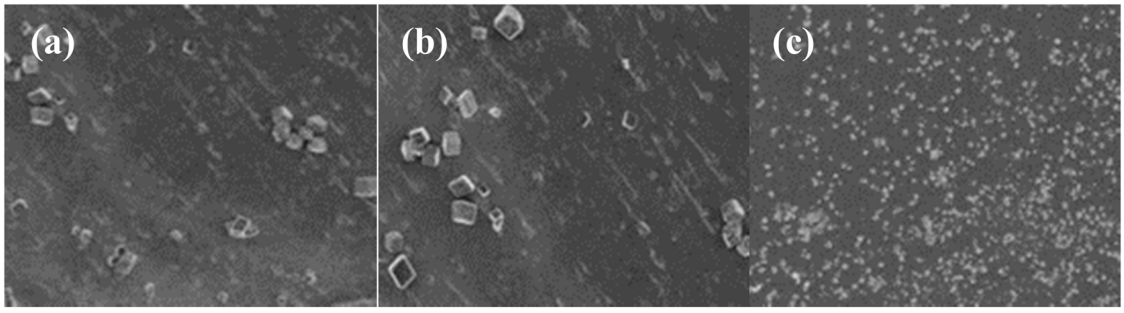

Figure 11: Effect of the melt temperature during water quenching on the microscopic morphology of the water-quenched samples at (a) 1,350°C, (b) 1,300°C, and (c) 1,220°C.

greater than the required minimum difference for fiber formation between the raw material melt temperature and its upper-temperature limit for crystallization.

3.5 Properties of $CaO–SiO_2–Al_2O_3$ inorganic fibers

Based on Al, Si, and Ca, which are the main elements of the melting-separated red mud, a ternary phase diagram for $CaO–SiO_2–Al_2O_3$ was constructed to analyze the theoretical problems in the preparation of inorganic fibers. The $CaO–SiO_2–Al_2O_3$ phase diagram includes composition systems of a series of silicate and red mud products; the schematic phase diagram is shown in Figure 12.

Inorganic fibers have an amorphous glass structure formed by melting and quenching. According to the theory of irregular networks, the melting-separation red mud contains Si^{4+} and Al^{3+}, which form tetrahedral structures in which the top corners are connected to form a three-dimensional spatial continuous network, and the basic conditions to form amorphous glass structures are satisfied. Figure 12 shows that if the melting-separated red mud is subjected to component reconstruction with the principle that an increase in the silicon content, a decrease in the aluminum content, and a moderate increase in the calcium content to achieve conversion to amorphous glass and acid slag composition region, it is possible to prepare $CaO–SiO_2–Al_2O_3$ inorganic fibers using the melting-separated red mud as the main raw material.

With the principle that an increase in the silicon content, a decrease in the aluminum content, and a moderate

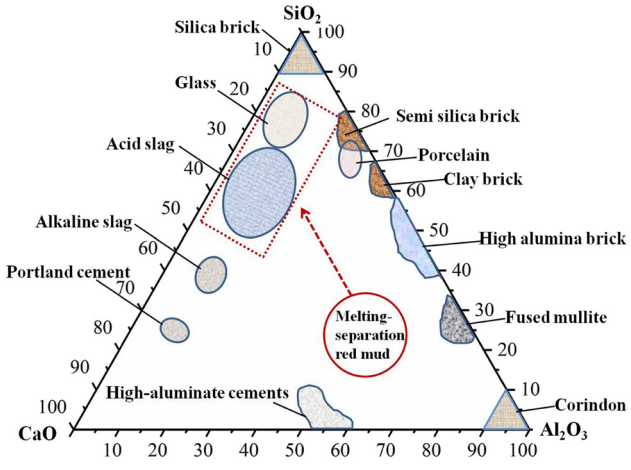

Figure 12: Composition of important silicate products in the $CaO–SiO_2–Al_2O_3$ phase diagram.

Table 2: Amount of the three additives added, experimental parameters, and fiber properties

Number	Amount added (%)			Main chemical components of molten modified melting-separated red mud (wt%)			Experimental parameters			Fiber properties	
	Melting-separated red mud	Dolomite	Quartz sand	SiO_2	CaO	Al_2O_3	Slagging temperature (°C)	Holding time (min)	Rotating speeds of rollers (rpm)	Fiber diameter (μm)	Slag ball content (%)
1	50	22.5	27.5	41.13	15.9	16.16	1,599	30	1#2707 2#3093 3#4350 4#5800	5.5	2.9
2	70	9	21	40.04	11.70	22.60	1,523	30		5.7	4.4
3	100	0	0	27.26	10.62	32.31	1,450	30		8.0	6.0

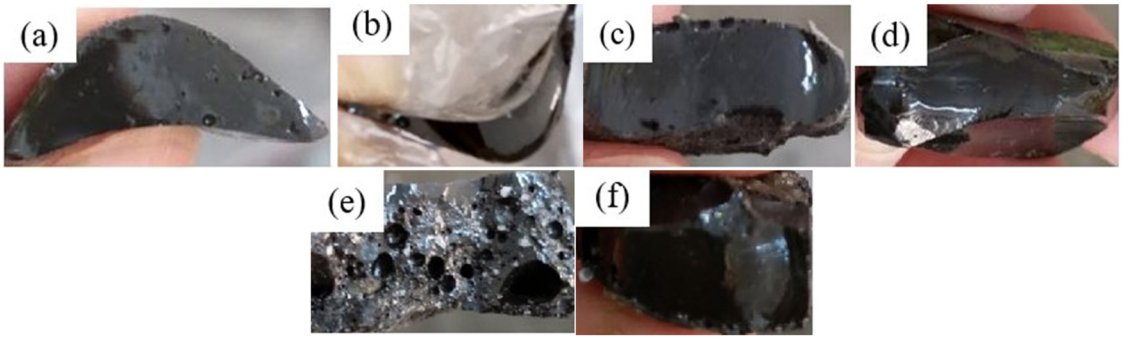

Figure 13: Effect of the holding time before fiber forming on the macroscopic morphology of the water-quenched samples. (a) The amount of the melting-separated red mud added was 50% and the holding time was 15 min; (b) the amount of the melting-separated red mud added was 50% and the holding time was 30 min; (c) the amount of the melting-separated red mud added was 70% and the holding time was 15 min; (d) the amount of the melting-separated red mud added was 70% and the holding time was 30 min; (e) the amount of the melting-separated red mud added was 100% and the holding time was 15 min; and (f) the amount of the melting-separated red mud added was 100% and the holding time was 30 min.

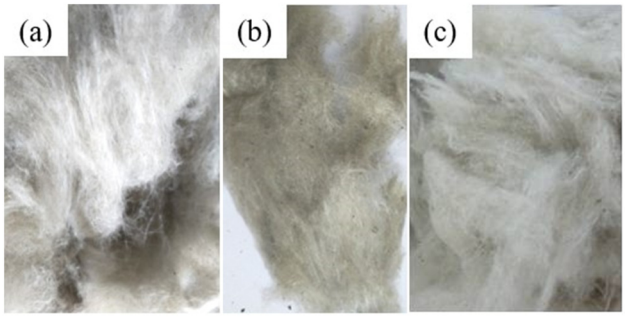

Figure 14: Photographs of $CaO–SiO_2–Al_2O_3$ inorganic fibers: (a) The amount of the melting-separated red mud added was 50%; (b) the amount of the melting-separated red mud added was 70%; and (c) the amount of the melting-separated red mud added was 100%.

increase in the calcium content, the melting-separated red mud, dolomite (with a composition of 47.06% CaO and 34.16% MgO), and quartz sand were used as raw materials to prepare inorganic fibers including modifying and fiber forming process; the proportions of the three additives, experimental parameters, and fiber properties are shown in Table 2. The effect of the holding time before fiber forming on the macroscopic morphology of the water-quenched samples is shown in Figure 13, and it can be seen that the modified melting-separated red mud was completely melted and homogeneous when the holding time was 30 min when different amounts of melting-separated red mud were added.

The macromorphology of the inorganic fibers is shown in Figure 14. The fibers had smooth surfaces and were arranged in a crossed manner at the macroscopic level; their color was grayish-white, and small quantities of slag balls were doped inside the fibers. In addition, with the increase in the added amount of the melting-separated red mud from 50 to 100%, the average fiber diameter increased from 5.5 to 8.0 μm. When the added amount of the melting-separated red mud was 50 and 70%, the average fiber diameter was less than 6 μm, which met the requirements of GB/t11835-2016. At the same time, it is superior to the properties of the slag cotton made by Balomenos et al. [40]. With the increase in the added amount of the melting-separated red mud from 50 to 100%, the slag ball content increased from 2.9 to 6.0%. The content of all of them was less than 7%, meeting the requirements of GB/t11835-2016. The average fiber diameter and slag ball content of the fiber prepared with the melting-separated red mud could be effectively reduced and the fiber quality could be significantly improved when the melting-separated red mud was subjected to a modifying treatment with the principle that an increase in the silicon content, a decrease in the aluminum content, and a moderate increase in the calcium content. This shows that the modifying principle in the process of preparing the inorganic fiber with melting-separated red mud is correct.

4 Conclusions

1) The main components of the melting-separated red mud were Al_2O_3, SiO_2, Fe_2O_3, CaO, Na_2O, TiO_2, and MgO, which satisfied the basic composition conditions required to prepare inorganic fibers with amorphous glass structures. The phase composition of the melting-separated red mud that underwent natural cooling in the air included $NaAlSiO_4$, $CaTiO_3$, Mg_2SiO4, and $(Mg, Fe)_2SiO_4$.

2) The decomposition reaction occurred in the temperature range from 900 to 1,250°C during the melting process of the melting-separated red mud. The melting time of the melting-separated red mud was 51 min, while the required time for the silicate formation process was 49 min. Therefore, the formation of the eutectic phase should be considered during composition reconstruction to shorten the silicate formation process during the inorganic fiber preparation process. Furthermore, the raw materials should be subjected to sufficient heat preservation at 1,250°C to reduce energy consumption during production.
3) The melting temperature of the melting-separated red mud was approximately 1,236°C, and the minimum suitable fiber-forming temperature and crystallization temperature of the melting-separation red mud melt were 1,433 and 1,350°C, respectively. This indicates that there is a big difference between the temperature for fiber formation and the upper limit crystallization temperature of the melt. In the high-temperature region with a suitable fiber formation viscosity, the melt had good fluidity. From the perspective of the temperature distribution of melt properties, the preparation of inorganic fibers from the melting-separated red mud is feasible.
4) It is feasible to prepare inorganic fibers from the melting-separated red mud but the composition should be reconstructed. The melting-separated red mud was subjected to component reconstruction with the principle that an increase in the silicon content, a decrease in the aluminum content, and a moderate increase in the calcium content. The melting-separated red mud was subsequently combined with two modifying agents (quartz sand and light burnt dolomite) and was used to prepare $CaO–SiO_2–Al_2O_3$ inorganic fibers under laboratory conditions. The fibers prepared from modified melting-separated red mud by adding different amounts of melting-separated red mud have smooth surfaces and are arranged in a crossed manner at the macroscopic level. Their color is grayish-white, and small quantities of slag balls are doped inside the fibers. With the increase in the amount of melting-separated red mud from 50 to 100%, the average diameter of the fibers increases from 5.5 to 8.0 μm, and the slag ball content increases from 2.9 to 6.0%. When the melting-separated red mud was modified with the principle that an increase in the silicon content, a decrease in the aluminum content, and a moderate increase in the calcium content, both the average diameter and slag ball content of the fibers increase, and the fiber quality could be significantly improved.

Acknowledgments: The authors are grateful for financial support from the National Science Foundation of China (51874138), Hebei Postgraduate Innovation Funding (CXZZBS2020135).

Funding information: This research was funded by National Science Foundation of China (51874138), Hebei Postgraduate Innovation Funding (CXZZBS2020135).

Author contributions: Peipei Du and Lei Xing: writing – original draft, writing – review and editing, methodology, and formal analysis. Yuzhu Zhang and Yue Long: writing – original draft, formal analysis, visualization, and project administration.

Conflict of interest: Authors state no conflict of interest.

References

[1] Archambo, M. and S. K. Kawatra. Red mud: fundamentals and new avenues for utilization. *Mineral Processing and Extractive Metallurgy Review*, Vol. 42, 2021, pp. 427–450.
[2] Huang, L. X., C. L. Li, H. B. Wang, X. X. Li, Y. R. Qi, and X. C. Zhu. Research progress on comprehensive utilization of red mud. *Journal of Physics: Conference Series*, Vol. 2009, 2021, pp. 1–6.
[3] Jing, W. B. Study on utilization of red mud solid waste resources. *Energy for Metallurgical Industry*, Vol. 40, 2021, pp. 7–10.
[4] Bao, H. M. and T. Fu. Analysis of comprehensive utilization of red mud. *Multipurpose Utilization of Mineral Resources*, Vol. 39, 2018, pp. 6–12.
[5] Jiang, C. C. *Study on modification of red mud and its application in lightweight thermal insulating wall materials*. Master's thesis, University of Jinan, Shandong, 2016.
[6] Park, H. S. and J. H. Park. Vitrification of red mud with mine wastes through melting and granulation process–Preparation of glass ball. *Journal of Non-Crystalline Solids*, Vol. 475, 2017, pp. 129–135.
[7] Xia, F., S. C. Cui, and X. P. Pu. Summary of the status quo of comprehensive utilization of red mud. *China Resources Comprehensive Utilization*, Vol. 39, 2021, pp. 85–89, 105.
[8] Qian, J. T., W. H. Li, and Y. Z. Zhang. Present situation of comprehensive utilization technology of red mud and development of new technology. *Guangdong Chemical Industry*, Vol. 43, 2016, pp. 122–123.
[9] Li, B., B. H. Zhang, P. Ning, L. W. He, and X. L. Zuo. Present status and prospect of red mud resource utilization and safety treatment. *Chemical Industry and Engineering Progress*, Vol. 37, 2018, pp. 714–723.
[10] Li, Y. J., H. Zhang, Y. X. Han, X. Liu, S. Yuan, and P. Gao. Research progresson resource recycling and utilization of red mud. *Metal Mine*, Vol. 538, 2021, pp. 1–19.
[11] Liu, S. H., X. M. Guan, S. S. Zhang, Z. Z. Dou, C. H. Feng, H. B. Zhang, et al. Sintered Bayer red mud based ceramic bricks:

Microstructure evolution and alkalis immobilization mechanism. *Ceramics International*, Vol. 43, 2017, id. 13004–13008.
[12] Li, R. B., T. G. Zhang, Y. Liu, G. Z. Lv, and L. Q. Xie. Calcification–carbonation method for red mud processing. *Journal of Hazardous Materials*, Vol. 316, 2016, pp. 94–101.
[13] Liu, D. Y., L. Hou, and P. Wang. Study on physicochemical features and the corresponding method for comprehensive utilization of common red muds. *Materials reports*, Vol. 26, 2012, pp. 310–312, 348.
[14] Khanna, R., Y. Konyukhov, D. Zinoveev, K. Jayasankar, I. Burmistrov, M. Kravchenko, et al. Red mud as a secondary resource of low-grade iron: A global perspective. *Sustainability*, Vol. 14, 2022, pp. 1–21.
[15] Liu, X., Y. X. Han, F. Y. He, P. Gao, and S. Yuan. Characteristic, hazard and iron recovery technology of red mud-A critical review. *Journal of Hazardous Materials*, Vol. 420, 2021, id. 126542–126542.
[16] Zinoveev, D. V., P. I. Grudinskii, V. G. Dyubanov, L. V. Kovalenko, and L. I. Leont'ev. Global recycling experience of red mud-A review. Part I: Pyrometallurgical methods. *Izvestiya Vysshikh Uchebnykh Zavedenij*, Vol. 61, 2018, pp. 843–858.
[17] Zinoveev, D., L. Pasechnik, M. Fedotov, V. Dyubanov, P. I. Grudinsky, and A. Alpatov. Extraction of valuable elements from red mud with a focus on using liquid media-A review. *Recycling*, Vol. 6, 2021, pp. 38–70.
[18] Gu, M. M. Research on key technology of comprehensive utilization of the red mud. *Light Metals*, Vol. 42, 2014, pp. 10–11, 16.
[19] Xing, L., P. P. Du, and Y. Long. Effect of SiO_2/Al_2O_3 on microstructure and thermal stability of inorganic fiber. *Journal of Iron and Steel Research*, Vol. 33, 2021, pp. 9–14.
[20] Wang, Y. L. *Study on the structure and properties of alkali resistant glass fiber prepared by red mud*. Master's thesis, University of Jinan, Shandong, 2018.
[21] Balomenos, E., I. Giannopoulou, D. Gerogiorgis, D. Panias, and I. Paspaliaris. Resource-efficient and economically viable pyrometallurgical processing of industrial ferrous by-products. *Waste and Biomass Valorization*, Vol. 5, 2014, pp. 333–342.
[22] Wu, F. N. Investigation of the preparation of alkali resistant glass fiber using blast furnace slag and other industrial waste. *Master's thesis*, University of Jinan, Shandong, 2016.
[23] Chang, Z. Y. *Investigation of the imitative basalt fiber prepared by red mud*. Master's thesis, University of Jinan, Shandong, 2016.
[24] Youngjae, K., K. Minseuk, S. Jungsoo, and P. Hyunsik. Applicability of gold tailings, waste limestone, red mud, and ferronickel slag for producing glass fibers. *Journal of Cleaner Production*, Vol. 203, 2018, pp. 957–965.
[25] Zhao, Y. Z. and H. R. Yin. *Glass technology*, 2nd edn, Chemical Technology Press, Beijing, China, 2016, pp. 26–31.
[26] He, P., D. C. Ju, P. F. Shen, and H. B. Jin. Experimental research on comprehensive utilization of red mud based on direct reduction and melting by RHF iron bead technology. *Energy for Metallurgical Industry*, Vol. 36, 2017, pp. 57–60.
[27] Li, S. Study on the resource utilization of Bayer red mud by carbothermic reduction. *Master's thesis*, Northeastern University, Liaoning, 2016.
[28] Li, Z. H. Fibering mechanism of modified molten blast furnace slag and experimental research. *Doctor's thesis*, Northeastern University, Liaoning, 2016.
[29] Wang, H., J. S. Wang, J. Liu, and Q. G. Xue. Experimental research on comprehensive utilization of the high iron red mud based on direct reduction and melting by RHF iron bead technology. *Light Metals*, Vol. 41, 2013, pp. 19–22.
[30] Farmer, V. C., B. F.L. Smith, M. J. Wilson, P. J. Loveland, and R. W. Payton. Readily-extractable hydroxyaluminium interlayers in clay- and silt-sized vermiculite. *Clay Minerals*, Vol. 23, 1988, pp. 271–277.
[31] Vedder, W. and R. S. Mcdonald. Vibrations of OH ions in muscovite. *Journal of Chemical Physics*, Vol. 38, 1963, pp. 1583–1595.
[32] Arab, M., D. Bougeard, and K. S. Smirnov. Experimental and computer simulation study of the vibrational spectra of vermiculite. *Physical Chemistry Chemistry Chemical Physics*, Vol. 4, 2002, pp. 1957–1963.
[33] Farmer, V. C., J. D. Russell, W. J. Mchardy, A. C.D. Newman, J. L. Ahlrichs, and J. Y.H. Rimsaite. Evidence for loss of protons and octahedral iron from oxidized biotites and vermiculites. *Mineralogical Magazine*, Vol. 38, 1971, pp. 121–137.
[34] Sroda, M. and C. Paluszkiewicz. The structural role of alkaline earth ions in oxyfluoride aluminosilicate glasses-Infrared spectroscopy study. *Vibrational Spectroscopy*, Vol. 48, 2008, pp. 246–250.
[35] Hamilton, J. P., S. L. Brantley, C. G. Pantano, L. J. Criscenti, and J. D. Kubicki. Dissolution of nepheline, jadeite and albite glasses: toward better models for aluminosilicate dissolution. *Geochimica Et Cosmochimica Acta*, Vol. 65, 2001, pp. 3683–3702.
[36] Corbridge, D. E.C. and E. J. Lowe. The infra-red spectra of some inorganic phosphorus compounds. *Jchemsoc*, Vol. 1, 1954, pp. 493–502.
[37] Zhang, Y. M., J. B. Li and Z. Z. Jiang. *Glass Fibre and Mineral Wool Encyclopedia*, 1st edn, Chemical Industry Press, Beijing, China, 2001, p. 639.
[38] He, K. K. *Guisuanyan Wuli Huaxue*, 2nd edn, Wuhan University of Technology Press, Wuhan, China, 2010, pp. 218–219.
[39] Li, L. X. and R. Jia. *Physical Chemistry of Silicate*, 2nd edn, Tianjin University Press, Tianjin, China, 2016, pp. 111–112.
[40] Balomenos, E., I. Gianopoulou, D. Panias, and I. Paspaliaris. A novel red mud treatment process: process design and preliminary results. *ISCOBA Conference 2011 India*, Vol. 36, 2011, pp. 255–266.